# The Influence of Iron in Minimizing the Microstructural Anisotropy of Ti-6Al-4V Produced by Laser Powder-Bed Fusion

MARCO SIMONELLI, DAVID GRAHAM MCCARTNEY, PERE BARRIOBERO-VILA, NESMA T. ABOULKHAIR, YAU YAU TSE, ADAM CLARE, and RICHARD HAGUE

There remains a significant challenge in adapting alloys for metal-based additive manufacturing (AM). Adjusting alloy composition to suit the process, particularly under regimes close to industrial practice, is therefore a potential solution. With the aim of designing new Ti-based alloys of superior mechanical properties for use in laser powder-bed fusion, this research investigates the influence of Fe on the microstructural development of Ti-6Al-4V. The operating mechanisms that govern the relationship between the alloy composition (and Fe in particular) and the grain size are explored using EBSD, TEM, and *in situ* high-energy synchrotron X-ray diffraction. It was found that Fe additions up to 3 wt pct lead to a progressive refinement of the microstructure. By exploiting the cooling rates of AM and suitable amount of Fe additions, it was possible to obtain microstructures that can be optimized by heat treatment without obvious precipitation of detrimental brittle phases. The resulting microstructure consists of a desirable and well-studied fully laminar $\alpha + \beta$ structure in refined prior-$\beta$ grains.

## I. INTRODUCTION

LASER powder-bed fusion (L-PBF) of structural alloys is beginning to find widespread use in a variety of applications thanks to the ability to produce net-shaped components with unparalleled design freedom. To sustain the development of this emerging manufacturing technology, a number of studies have investigated how the unique microstructure imposed by L-PBF affects the macroscale mechanical properties of important engineering alloys, in particular those based on titanium such as Ti-6Al-4V.

The microstructure of Ti-6Al-4V after L-PBF exhibits complex features that span across several length scales (from the nm to mm scale), the morphology, and arrangement of which are influenced by the printing process, such as the laser power, scanning speed, the spacing between raster paths (also known as hatch spacing), position within the part, the scan strategy, and the environmental conditions (temperature and oxygen concentration). Typically, a hierarchical structure made up of fine martensitic $\alpha'$ phase (including primary, secondary, tertiary, and quartic martensite plates) within columnar prior-$\beta$ grains dominates the microstructure of Ti-6Al-4V in the as-built L-PBF condition.[1] While the metastable $\alpha'$ phase can be readily decomposed into a more ductile $\alpha + \beta$ microstructure by standard post-processing heat treatments,[2,3] the columnar prior-$\beta$ grains maintain, however, a characteristic elongated morphology. This morphology is an undesirable feature of L-PBF, and more generally in additively made materials. Such columnar prior-$\beta$ grains are known to negatively affect the mechanical properties of Ti-6Al-4V, giving rise to anisotropy and low fracture toughness and consequently affecting the fracture modes and fatigue resistance of the alloy.[4–8]

The formation of columnar prior-$\beta$ grains and, more specifically, their suppression, *via* suitable modification of the alloy chemistry of Ti-6Al-4V, is the focus of this present study.

The formation of columnar prior-$\beta$ grains in Ti-6Al-4V is a consequence of epitaxial growth (from

MARCO SIMONELLI, NESMA T. ABOULKHAIR, and RICHARD HAGUE are with the Centre for Additive Manufacturing, University of Nottingham, Nottingham, NG8 1BB, UK. Contact e-mail: Marco.Simonelli@nottingham.ac.uk DAVID GRAHAM MCCARTNEY is with the Advanced Materials Group, University of Nottingham, Nottingham NG7 2RD, UK. PERE BARRIOBERO-VILA is with the Institute of Materials Research, German Aerospace Center (DLR), Linder Höhe, Cologne, 51147, Germany. YAU YAU TSE is with the Department of Materials, Loughborough University, Loughborough, LE11 3TU, UK. ADAM CLARE is with the Advanced Component Engineering Laboratory (ACEL), University of Nottingham, Nottingham NG7 2RD, UK.
Manuscript submitted October 21, 2019.

a substrate of previously deposited layers) of the high-temperature $\beta$ phase during the layer-by-layer deposition.[9] It is now accepted that, in a repeating sequence, as a new layer of powder is melted, the top of the previously deposited layer is also re-melted; the melt pool does therefore solidify on pre-existing $\beta$ grains that are predominantly oriented with a $\langle 100 \rangle$ direction along the build direction. Under the high solidification speed ($R$) and temperature gradients ($G$) typical of L-PBF, nucleation events in the melt pool are largely prevented. This gives rise to epitaxial growth from the underlying substrate and planar/dendritic grain solidification mode of elongated grains with $\langle 100 \rangle$ along the dominant heat flow direction.[4]

Several studies have been carried out with the aim of suppressing the formation of $\beta$ columnar grains in laser-based additive processing of titanium. The approaches taken in the literature can be broadly divided into: (a) manipulation of the processing space to reduce $G/R$, (b) post-processing heat treatments below and above the $\beta$ transus temperature, and (c) modification of the alloy constituents to promote the columnar to equiaxed transition (CET) during solidification.

Manipulation of the parameter space and beam shaping are interesting approaches that have been used to promote the CET.[10,11] In the case of Ti-6Al-4V, useful solidification maps have been built to predict the effect of laser parameters on the dominant grain structure morphology for a variety of beam deposition and electron beam additive processes.[12,13] Nevertheless, these are not always practical or possible approaches as the ultimate aim of L-PBF is the creation of fully dense components of any arbitrary geometry and indeed evidence suggests limited success in forming dense Ti alloys with an equiaxed microstructure.[14]

Studies have demonstrated that sub-transus heat treatments are ineffective in changing the morphology of the prior-$\beta$ grain boundaries, as the retained $\alpha$ phase effectively pins the $\beta$ grain boundaries already present in the structure.[15] A full $\beta$-solution heat treatment (above the $\beta$ transus temperature) has instead shown that $\beta$ grain boundaries can migrate and split realizing equiaxed structures but these treatments lead to inevitable coarsening of the structure at the expense of ductility and strength.[15,16]

Great effort has also been spent in modifying the constitution of Ti-6Al-4V to control the solidification mode of the high-temperature $\beta$ phase. Recognizing that Al and V provide limited constitutional undercooling in Ti-6Al-4V alloys,[17] and building on the growth restriction theory developed for casting,[18] a number of solutes with high-growth restriction factor ($Q$) in Ti have been investigated ($Q = m_l c_0 \cdot (k - 1)$, where $m_l$ is the slope of the liquidus line on the phase diagram (K/wt pct), $c_0$ is the solute concentration in the corresponding binary alloy (wt pct), and $k$ is the partition coefficient of the added solute).

A promising solute for refining prior-$\beta$ grains in Ti alloys is silicon (Si). Si has proven to be an effective grain refiner in cast commercially pure (cp-) Ti and Ti-6Al-4V although there is contrasting evidence on whether intermetallic silicides might form during primary solidification and how these affect the mechanical properties of the resulting alloy.[19,20] Mereddy et al. have recently investigated the addition of Si to wire arc additively manufactured cp-Ti and have suggested a mechanism where Si solute segregation hinders lateral growth of $\beta$ grains, resulting in $\beta$ grains that maintain high-aspect ratio but are effectively refined in width.[21] Beryllium (Be) that has the highest theoretical $Q$ as a solute addition to Ti has produced significant grain refinement, although its use as a grain refiner in additive manufacturing (AM) might be limited due to associated health hazards.[22] Molybdenum (Mo) has been shown to expand the freezing range of Ti-6Al-4V, destabilize the planar growth of Ti-6Al-4V, and reduce the size of the prior-$\beta$ grains.[17] Mo particles are, however, generally retained in the microstructure as a result of the thermo-physical property differences with Ti causing microstructural and chemical inhomogeneities that can lead to undesirable scatter in mechanical properties.[23,24] Additionally, partial dissolution of Mo is intrinsically linked to relatively low efficiency, as a large amount of Mo seems not to take part in the solidification process. Chromium (Cr) has also been considered as a grain refiner for Ti.[18,25] Although research on casting demonstrated that during the primary solidification Cr super-saturates $\alpha + \beta$ phases, the complex thermal history of laser AM processing has been shown to produce grain boundary precipitates in the form of $TiCr_2$ Laves phases that have a deleterious effect on the properties of the alloy.[26,27]

In other approaches, the coupled action of both solutes with high $Q$ and heterogeneous nuclei in the form of insoluble substrates has also been explored. Boron (B),[28,29] tungsten (W)[30], and a number of rare-earth elements (La, Y, etc.)[31-33] have been shown to affect the phase transformation and produce a significant constitutional undercooling and an increase in the nuclei population to encourage equiaxed grain formation in Ti and Ti-based alloys. Nevertheless, although B has a large $Q$, its use as a grain refiner may be limited when its deleterious effect on ductility caused by the precipitation of titanium borides is considered. Rare-earth oxides and W have been shown to be stable compounds in liquid Ti and thus promising candidates for heterogeneous nucleation of Ti grains. However, after laser AM, the resulting composite microstructure consists of heterogeneous particles distributed within the typical $\alpha + \beta$ microstructure of Ti alloys suggesting poor nucleation efficiency. The distribution of these secondary phases in the microstructure and their effect on the mechanical properties of the alloy is still a matter of ongoing research but appears largely deleterious.

While recognizing the importance, and most likely the necessity, of introducing potent heterogeneous nucleation substrates for promoting CET in laser AM—particularly L-PBF that is characterized by extremely high $G$ and $R$ values—the identification of suitable solute additions that refine prior-$\beta$ grains without forming deleterious brittle phases remains a scientific challenge in

AM and other energy beam-processing methods used to manufacture Ti-based alloys.

The purpose of the present study is to elucidate the influence of iron (Fe) on microstructure formation in a modified Ti-6Al-4V alloy containing Fe as a quaternary solute and to evaluate its suitability for producing a refined grain structure. Fe is characterized by a high $Q$ value that directly favors the creation of constitutional undercooling (a pre-requisite for the CET),[25,34] unfavorable kinetics for the formation of brittle intermetallics,[35] and thermo-physical properties comparable to Ti that would encourage homogeneous mixing during L-PBF.[23] Accounting for all these considerations, Fe is potentially a suitable alloy component in Ti-6Al-4V to refine the grain structure while maintaining a well-characterized and predictable balance of $\alpha$ and $\beta$ phases in the final microstructure.

## II. MATERIALS AND METHODS

### A. Powder Feedstock and Alloy Selection

Pre-alloyed plasma atomized Ti-6Al-4V powders (Carpenter AM) of spherical morphology and with size distribution D10 = 22.1 $\mu$m, D50 = 33.5 $\mu$m, and D90 = 49.9 $\mu$m were used as the reference material. Additionally, three Ti-6Al-4V + Fe powder feedstocks were prepared to assess the efficiency of Fe as quaternary addition to promote a refined grain structure. The Ti-6Al-4V + Fe feedstocks were prepared by decorating the reference material (pre-alloyed Ti-6Al-4V) with 99.9 pct pure Fe particles (GoodFellow Cambridge Limited) of size distribution D10 = 2.9 $\mu$m, D50 = 5.7 $\mu$m, and D90 = 12.7 $\mu$m using the satelliting method described elsewhere.[36] Prior to the L-PBF printing process, all feedstock materials were dried overnight at 100 °C to minimize the moisture content. Thermogravimetric analysis (TGA) up to 600 °C indicated that polymeric residues from the satelliting method could not be detected in any of the powder feedstocks prior to printing.

The range of Fe additions was studied in accordance with thermodynamic calculations to estimate the solidification range and partitioning effect of solutes in the Ti-6Al-4V system using ThermoCalc software and the commercially available SSOL5 database. The accuracy of the thermodynamic calculations was assessed by comparing corresponding calculated and experimental binary phase diagrams extracted from Reference 37. To assess the contribution of each solute to $Q$, the slopes of the liquidus lines were estimated from the Ti-rich portion of the calculated binary diagrams (solute level between 0 and 10 wt pct). The partition coefficient $k$ for the addition of Fe from 1 to 4 wt pct is instead calculated under equilibrium conditions at the liquidus temperature. The solidification range is evaluated under Scheil conditions on the ternary and quaternary alloys investigated in this research. The calculation was terminated at solid fraction of 0.8 as beyond this point the formation of peritectic TiFe is erroneously predicted (no TiFe was experimentally observed in the samples).

Three compositions were prepared so that for every equivalent of 100 g of total material, 2, 3, or 4 g of Fe would be added to the remaining balance of pre-alloyed Ti-6Al-4V (for simplicity, the formulations will be expressed throughout the paper with a compact notation of the form: Ti-6Al-4V-xFe, where $x$ varies between 2 and 4). This range of compositions was used to conduct a preliminary assessment and establish the point beyond which further additions of Fe did not lead to further significant refinement of the prior-$\beta$ grains as determined by optical microscopy.

### B. L-PBF Manufacturing Process and Heat Treatments

The microstructural investigations were carried out on cubic samples (10 mm) manufactured on a Renishaw AM400 which allowed the investigation of the microstructural formation under regimes close to that used in industrial practice. The AM400 was operated using the reduced build volume configuration with a laser power of 300W, 70 $\mu$m hatch spacing, 50 $\mu$m layer thickness, and 750 mm/s scan speed (point distance of 80 $\mu$m). This parameter set was derived from previous studies on the densification of Ti-6Al-4V. Each layer was melted once. The laser scan direction was then rotated by 90 deg between each two consecutive layers to ensure equal scan vector lengths per cross-section. All samples were built on Ti-6Al-4V build plates which were not preheated. The process chamber atmosphere was regulated with circulating Ar to keep oxygen levels below 0.09 pct. Samples were fabricated symmetrically across the build plate to ensure that the results were not affected by the build position. The melt pool size formed under these processing conditions was estimated from cross-sectional images of scan tracks of pre-alloyed Ti-6Al-4V substrate. Under such processing conditions, key-hole melting regime took place. This ensured both adequate mixing of Fe during melting and a high material density (above 99.8 pct, estimated via optical microscopy). Three specimens were then heat treated to study the decomposition of the as-built microstructure at high-temperature. Prior to heat treatment, the samples were enclosed in evacuated quartz tubes. The heat treatment was carried out at 900 °C for 4 hours and was followed by furnace cooling consistently with most HIP treatments reported in the literature which are performed in the high portion of the $\alpha/\beta$ phase field.[4]

### C. Microstructural Characterization

To obtain representative microstructures, specimens were mechanically ground and polished. Kroll's reagent (5 mL HF, 6 mL HNO$_3$, and 89 mL H$_2$O) was used to etch the samples to reveal the microstructure on three orthogonal planes in agreement to that suggested in the ISO/ASTM 52921 standard.[38] The etched samples were imaged using a Nikon Eclipse LV100ND optical microscope. Electron backscatter diffraction (EBSD) coupled with energy-dispersive spectroscopy (EDS) was carried out on a Helios G4 PFIB UXe DualBeam Microscope FIB/SEM to resolve the grain structure, the elemental distribution, and crystallographic texture of the samples.

The EBSD analysis was carried out on the frontal planes (*xz*-plane with reference to Reference 38) of the deposited structure using HKL-Channel 5™ software package and the MATLAB™ toolbox MTEX. The inverse pole figures were plotted along the *z*-axis, with the *z*-axis parallel to the building direction. From the EBSD maps, individual grains were identified as regions completely bounded by interfaces with misorientation angle larger than 8 deg, which is the typical maximum misorientation spread measured in prior-$\beta$ grains observed in L-PBF Ti-6AL-4V.[9] This led to the identification of 1534 $\beta$ grains. It was then possible to automatically calculate the area of each grain and its aspect ratio (defined as the ratio between the major and minor axis of the fitted ellipse). The orientation relationship between $\alpha$ and $\beta$ phases was studied on orientation maps acquired with a step size of 0.1 $\mu$m, given the expected fine size of the $\alpha/\alpha'$ laths.

Samples for Transmission Electron Microscopy (TEM) were prepared using a FEI Quanta 200 3D Dual Beam FIB-SEM. A JOEL 2000FX was used to carry out the TEM investigations. The phase identification in the bulk samples was investigated by X-Ray Diffraction (XRD) using a Bruker D500 X-ray diffractometer using Cu K-$\alpha$ radiation (0.15406 nm wavelength) from the frontal plane of the samples. A step time of 20 second and step size of 0.03 deg were used for all scans.

*In situ* high-energy synchrotron X-ray diffraction (HEXRD) was carried out to at the P07-HEMS beamline of PETRA III (Deutsches Elektronen-Synchrotron) as described in detail in Reference 32. The phase transformation kinetics of the material in the L-PBF as-built condition was investigated during continuous heating and cooling rates of 100 °C/min between room temperature and 1000 °C (*i.e.*, up to a temperature close to the $\beta$ transus). An energy of 100 keV ($\lambda$ = 0.0124 nm) was used. The acquisition time and sample-detector distance were 5 seconds and 1926 mm, respectively. The investigated samples were cut from the center of as-built SLM cubes and were investigated close to the center of the building height in transmission mode using a gauge volume of $0.8 \times 0.8 \times 5$ mm$^3$. The temperature was controlled by a spot-welded thermocouple located next to the position of the incident beam. Qualitative analysis of the evolution of the diffraction patterns was carried out by converting the Debye–Scherrer rings into Cartesian coordinates (Azimuthal angle $\psi$, $2\theta$). Subsequently, projection of the summed intensity of Bragg reflections on the $2\theta$ axis was performed using the software ImageJ. The instrumental parameters of the HEXRD setup were obtained using a LaB$_6$ powder standard.

## III. RESULTS

### A. *Preliminary Screening of Ti-6Al-4V-Fe Adaptations*

Three adaptations of Ti-6Al-4V were prepared by adding various amounts of pure Fe as described in Section II–A. The preliminary observations on the refinement caused by Fe additions are shown in Figure 1 where the microstructure of the frontal plane of the specimens is revealed by etching the metallurgically prepared surfaces (the build direction is indicated by white arrows).

Figure 1(a) shows a columnar microstructure typical of that observed in Ti-6Al-4V. With the addition of 2 wt pct Fe (Figure 1(b)), a significant refinement of the prior-$\beta$ grains is observed. As more Fe is added (Figure 1(c) and (d)), it is difficult to quantitatively discern any $\alpha$ plates and the prior-$\beta$ grain boundaries although an apparent change in the prior-$\beta$ grain morphology is evident. Using the planimetric method,[39] it was established that additions of up to 3 wt pct Fe led to significant refinement of the grains with little further benefit when the addition was increased to 4 wt pct and for this reason Ti-6Al-4V-3Fe was investigated in greater detail in the rest of the study.

### B. *Microstructure Analysis of the Ti-6Al-4V-3Fe As-Built Specimens*

The XRD spectra and optical micrograph composites in Figure 2 provide an overview of the typical microstructures of Ti-6Al-4V and Ti-6Al-4V-3Fe in the as-built condition.

In Figure 2(a), it can be observed that after L-PBF, the microstructure of Ti-6Al-4V consists of acicular $\alpha/\alpha'$ grains contained in columnar prior-$\beta$ grains predominantly aligned along the build direction (BD).[9] In Ti-6Al-4V-3Fe (Figure 2(b)), it is noted a significant redistribution of the peak intensities—with the intensities the $\alpha/\alpha'$ peaks decreasing at the expenses of the $\{110\}_\beta$, $\{200\}_\beta$ and $\{220\}_\beta$ peaks indicating that, following L-PBF, a significant amount of $\beta$ phase is retained in the specimens. In the corresponding micrographs, it can be observed that the $\beta$ grains show a mixture of apparent equiaxed and elongated morphologies. On the horizontal *xy*-plane, the cross-sections of the $\beta$ grains are observed with clear delineation of the laser scan tracks. The EDS area analysis reported in Table I indicate the average composition measured in the Ti-6Al-4V and Ti-6Al-4V-3Fe specimens. A reduced Fe content to the nominal value is most likely linked to the feedstock preparation and to the fact that given the particle size difference, Fe particles fused and partially evaporated first.[23]

To quantify the grain structure in the samples, large-scale EBSD was carried out (Figure 3).

The orientation maps reveal that the predominant structure is $\beta$ phase with localized precipitation of the small $\alpha/\alpha'$ colonies predominantly in periodic thin regions parallel to the build platform (white lines marked on the $\alpha$-orientation map). The $\beta$ orientation map shows that the morphology of the grain structure is non-uniform with apparent equiaxed morphology dominating the first few and last layers of the sample and a mixed columnar/equiaxed structure in the remaining areas. Most of the grains identified in the maps (approximately 65 pct of the entire grain population) have an aspect ratio $< 2$ and therefore have an apparent equiaxed morphology (as per Reference 40). Nevertheless, these are small grains that account for
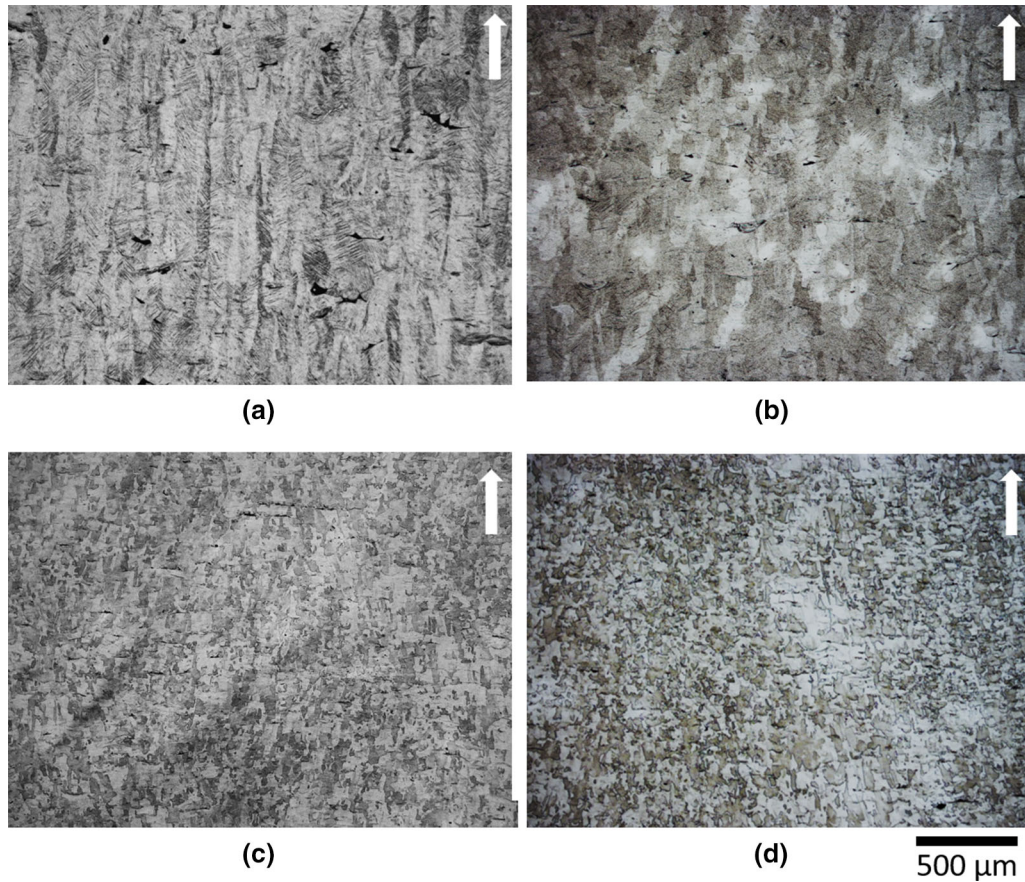
Fig. 1—Optical micrographs of as-built samples in the frontal plane of observation showing the typical microstructure of (*a*) Ti-6Al-4V, (*b*) Ti-6Al-4V-2Fe, (*c*)Ti-6Al-4V-3Fe, and (*d*) Ti-6Al-4V-4Fe. The white arrows indicate the building direction.

approximately only 30 pct of the area of the structure. Notably, however, 90 pct of the area of the structure consists of grains with an aspect ratio < 6 (gray markers in Figure 3), a critical empirical threshold that has been suggested to link anisotropic strain-to-failure and grain morphology.[41] The contour pole figure plots quantify the texture intensities of the $\beta$ phase for the three crystallographic plane families $\{001\}_\beta$, $\{110\}_\beta$ , and $\{111\}_\beta$ with respect to the frontal plane of the sample. The pole figures show a clear $\{001\}_\beta$ cube texture component rotated approximately by 15 deg to the building direction, which is consistent with the morphological orientation of the columnar grains observed in the microstructure. The contour pole figures calculated from a subset containing only the grains with apparent equiaxed morphology (aspect ratio < 2, light gray markers) still showed a similar cube texture component, although attenuated in intensity. To investigate in more detail the precipitation of the $\alpha/\alpha'$ phase higher-resolution orientation maps (step size 0.1 $\mu$m) where then acquired (Figure 4).

The analysis indicates that the $\alpha/\alpha'$ laths are arranged in small colonies or as a grain boundary (GB) $\alpha$ well delineated at the boundary between two prior-$\beta$ grains and on the melt pool boundaries. The comparison of the contour pole figures of the $\alpha/\alpha'$ and $\beta$ phases reveals that the two phases are mostly related by the Burgers Orientation Relationship (BOR), as indicated by the parallelism between the reflections associated with the $\{0001\}_\alpha/\{110\}_\beta$ and $\{11\bar{2}0\}_\alpha/\{111\}_\beta$ planes. The difference in the intensity distribution noticed in the parallel $\{0001\}_\alpha/\{110\}_\beta$ reflections indicates that variant selection is likely to occur during transformation. In addition, it is noticed that some of the reflections in the $\{110\}_\beta$ are missing from the corresponding $\{0001\}_\alpha$ contour pole figure (an example is marked by a dotted circle). This might be attributed to $\alpha/\alpha'$ laths that precipitate without obeying the BOR. It should be noted, however, that minor texture components might be obfuscated in the spherical harmonic representation of the texture and therefore studies of the individual grain orientation relationship are ongoing. Examples of conditions where BOR is not maintained include cases of simultaneous phase transformation and recrystallization of the $\beta$ matrix[42] and nucleation of $\alpha/\alpha'$ laths *via* peritectic reactions.[32] The complete understanding of the crystallography dependence on composition necessitates, however, further additional studies. Figure 5 shows the arrangement of the laths in the retained $\beta$ and the existence of a hierarchical structure with grains
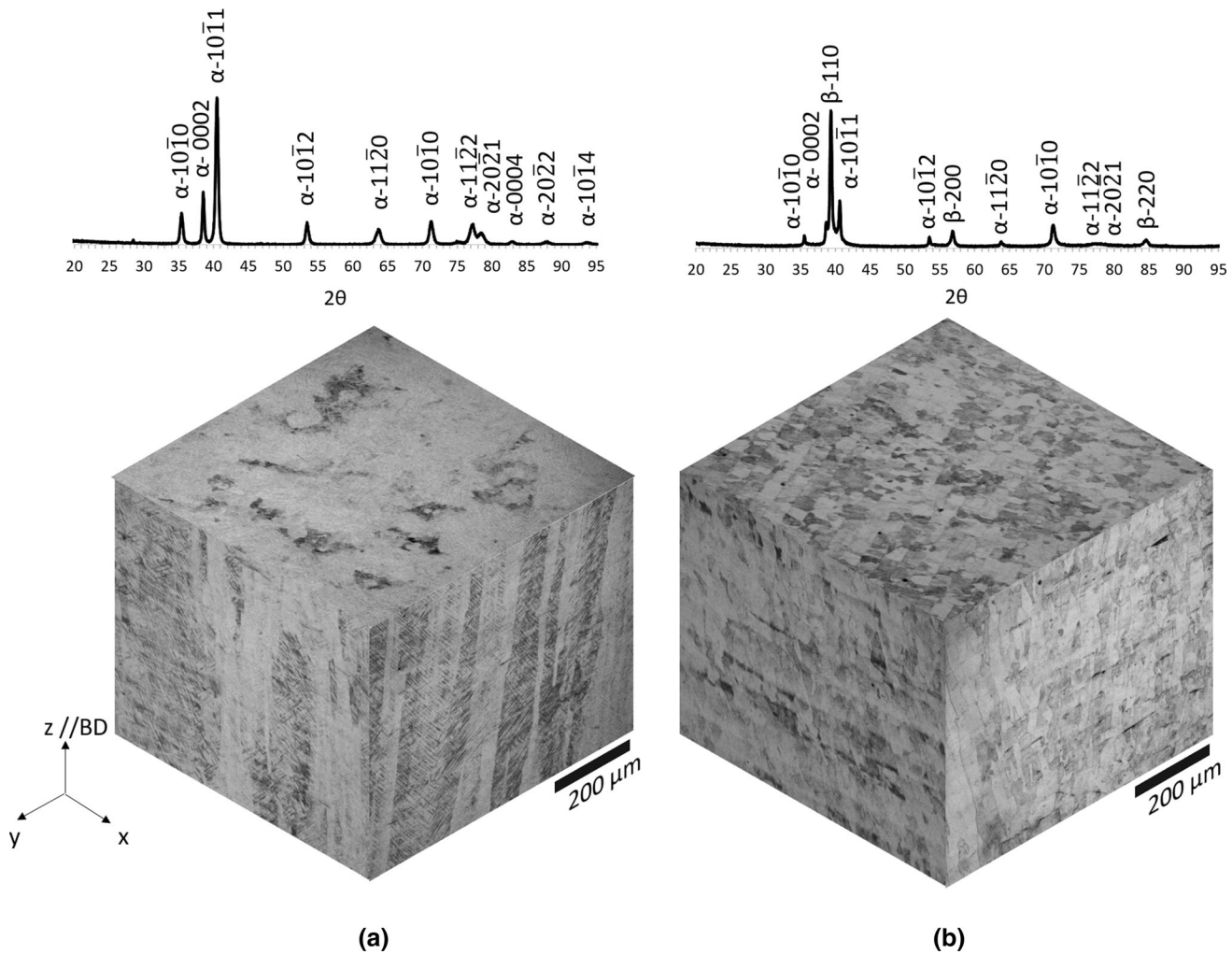
Fig. 2—XRD spectra and the corresponding optical micrograph composite images of as-built microstructure for (*a*) Ti-6Al-4V and (*b*) Ti-6Al-4V-3Fe produced under identical processing conditions. Comparison of the XRD spectra reveals the retention of some *β* phase in the Fe-containing alloy.

spanning the nm to the $\mu$m scale (indicated in Figure 5(b) by white arrows).

Selective area diffraction patterns (SADP) obtained from within individual laths confirm that these have an HCP structure and thus the likely martensitic $\alpha'$ nature of these precipitates. In addition, no other minor phases such as Fe-containing intermetallics or $\omega$-phase are observed in the structure. The analysis of the grain composition reveals that there is a marked difference in the partitioning behavior of V and Fe between the GB $\alpha$ (Figure 5(a)) and the neighboring $\alpha'$ laths (Table II). Nevertheless, in the areas of the microstructure where the $\alpha'$ and $\beta$ phases coexist (as indicated in Figure 5(c)), Fe partitions preferentially significantly in the $\beta$ phase. The morphology and the high solute content measured in the colonies suggest indeed the predominance of a martensitic $\alpha'$ phase in the as-built structure, which is not surprising considering the high cooling rates associated with the thermal cycles typical of L-PBF.

### C. Ti-6Al-4V-3Fe Microstructural Decomposition After Heat Treatment

*In situ* HEXRD was used to gain an understanding of the transformation mechanisms that occur in the Ti-6Al-4V-3Fe alloy during heating and cooling (100 °C/min) of the L-PBF as-built microstructure (Figure 6). The results indicate that during heating up to 450 °C, the microstructure remains composed of $\alpha/\alpha'$ and $\beta$ phase and negligible solute partitioning takes place as evidenced by the absence of a shift in the peaks positions. As temperature increases, in the range 450 °C to 700 °C, a change of the maximum intensity of the reflections of the two phases takes place: the intensity of $\{110\}_\beta$ decreases while that of $\{10\bar{1}1\}_\alpha$ increases indicating a $\beta \rightarrow \alpha$ transformation is occurring. In addition, the $\{110\}_\beta$ reflection shifts to higher $2\theta$ between 450 and 600 °C and then to lower $2\theta$ between 600 and 750 °C. These shifts in $2\theta$ are due to decrease and increase,

**Table I.   Average Composition of Ti-6Al-4V and Ti-6Al-4V-3Fe Determined by EDS Analysis**

| Material/Condition | Element (Wt Pct) | | | |
| --- | --- | --- | --- | --- |
| | Ti | Al | V | Fe |
| Ti-6Al-4V/As-Built | bal. | $6.2 \pm 0.1$ | $3.8 \pm 0.1$ | traces |
| Ti-6Al-4V-3Fe/As-Built | bal. | $5.7 \pm 0.2$ | $3.6 \pm 0.2$ | $2.6 \pm 0.3$ |

respectively, of the lattice parameter of the $\beta$ phase during heating. The effect is most likely associated with preferential solute partitioning. These results indicate that, as expected, the microstructure in the as-built condition is metastable and that upon heating the structure recovers towards a more stable one with phase fraction and phase compositions moving towards equilibrium values. As the temperature exceeds 700 °C, a further phase transformation is enabled, with $\alpha$ transforming to $\beta$ phase as expected from the equilibrium phase relationships. At approximately 900 °C, the microstructure consists almost exclusively of $\beta$ phase. Given these findings, it is clear that Fe acts as a $\beta$-phase stabilizer and, under L-PBF conditions, is responsible for promoting the retention of metastable $\beta$ in the microstructure. This directly translates to a marked decrease of the dissolution temperature of the $\alpha$ phase and the $\beta$ transus temperature of the new Ti-6Al-4V-3Fe alloy with respect to Ti-6Al-4V.[43]

To gain insight into the partitioning behavior of Fe in the alloy, it is useful to compare these results with those obtained from quenched martensitic wrought Ti-6Al-4V (with starting microstructure analogous to that of L-PBF condition). During heating of martensitic Ti-6Al-4V, we observed a marked shift of the $\{110\}_\beta$ reflection to lower $2\theta$ above 650 °C. This shift, associated with an expansion of the lattice parameter of $\beta$, is attributed to progressive reduction in the concentration of V from the $\beta$ phase and an enrichment in Ti.[43,44] In Ti-6Al-4V-3Fe, the first observed shift of the $\{110\}_\beta$ reflection towards higher $2\theta$ occurs in the temperature range 450 to 600 °C (temperatures at which no shifts occur in Ti-6Al-4V where no $\beta$ is present in the initial condition). The associated contraction in lattice parameter can only be explained considering a progressive Fe enrichment of the $\beta$ phase that can be justified taking into account the starting metastable microstructure induced by L-PBF and the relatively high diffusivity of Fe in Ti in comparison with Al and V.[35] By further increasing the temperature, the $\{110\}_\beta$ reflection then shifts towards lower $2\theta$, marking the dissolution of $\alpha$ through V transport across the $\beta/\alpha$ interface consistently to that observed in Ti-6Al-4V (no Fe).[43] Upon cooling from the $\beta$ field (1000 °C), the $\beta \rightarrow \alpha$ phase transformation initiates approximately at 800 °C. This is considerably lower than $\beta$ transus temperature observed during the first heating ramp, suggesting that $\beta$ annealing produces a complete equilibrium homogenization of the microstructure. No other events are showing in the intensity plots in Figure 6 for Ti-6Al-4V-3Fe, indicating

that no additional phase transformations (at least in the detectable range of HEXRD) occur in the alloy.

To further investigate the possibility of the formation of Fe-containing intermetallics or $\omega$-phase in Ti-6Al-4V-3Fe, detailed microstructural examination was conducted of samples that were heat treated at 900 °C for 4 hours and then furnace cooled (Figures 7 and 8). The EBSD-derived IPF orientation and phase maps in Figure 7 indicate that the microstructure of the alloy after heat treatment consists of a fully lamellar $\alpha + \beta$ with the prior $\beta$ grain boundaries decorated by GB $\alpha$.

The TEM bright-field images of Figure 8 show the arrangement of the phases in detail and it is notable that, intermetallic compounds are not observed in the structure. Precipitates were not found in the core of the $\alpha$ grains nor at the grain boundaries present in the microstructure (Figure 8 inset). In particular, $\omega$ phase cannot be detected in the microstructure. Only reflection from the $\beta$ phase is detected in the SADP at zone axis pattern $\langle 1\bar{1}0 \rangle_\beta$ as shown in Figure 8. The composition of the microstructural features given in Table III shows that Fe partitions almost exclusively in the $\beta$ phase and the Al and V content in the GB $\alpha$ show a larger scatter from the corresponding average than in the case of the primary $\alpha$.

## IV.  DISCUSSION

### A. *Refinement of the Microstructure Through Fe Additions*

The formation of equiaxed grains, an ideal condition for the formation of refined and isotropic microstructures, is associated to an equiaxed dendritic growth at the $S/L$ interface. It is typically promoted by a low thermal gradient ($G$) to growth rate ($R$) ratio.[40,45] In most cases, during L-PBF, $R$ approaches 1 m/s (in the present study the maximum solidification velocity can be approximate to the laser beam velocity of 0.75 m/s) while $G$ values are in the order of $10^6$ to $10^7$ K/m.[4,31] This leads to high $G/R$ ratios and therefore dendritic growth assumes the well-reported columnar/directional morphology. As it has been demonstrated by a number of investigations, this regime can be changed by the addition of (i) solutes with a high-growth restriction factor $Q$ and (ii) potent heterogeneous nuclei that can act as substrates for $\beta$-phase nucleation from the melt. Given the reactivity of liquid titanium, however, several high $Q$ solutes nucleate as intermetallic compounds thus ceasing to contribute to the development of a
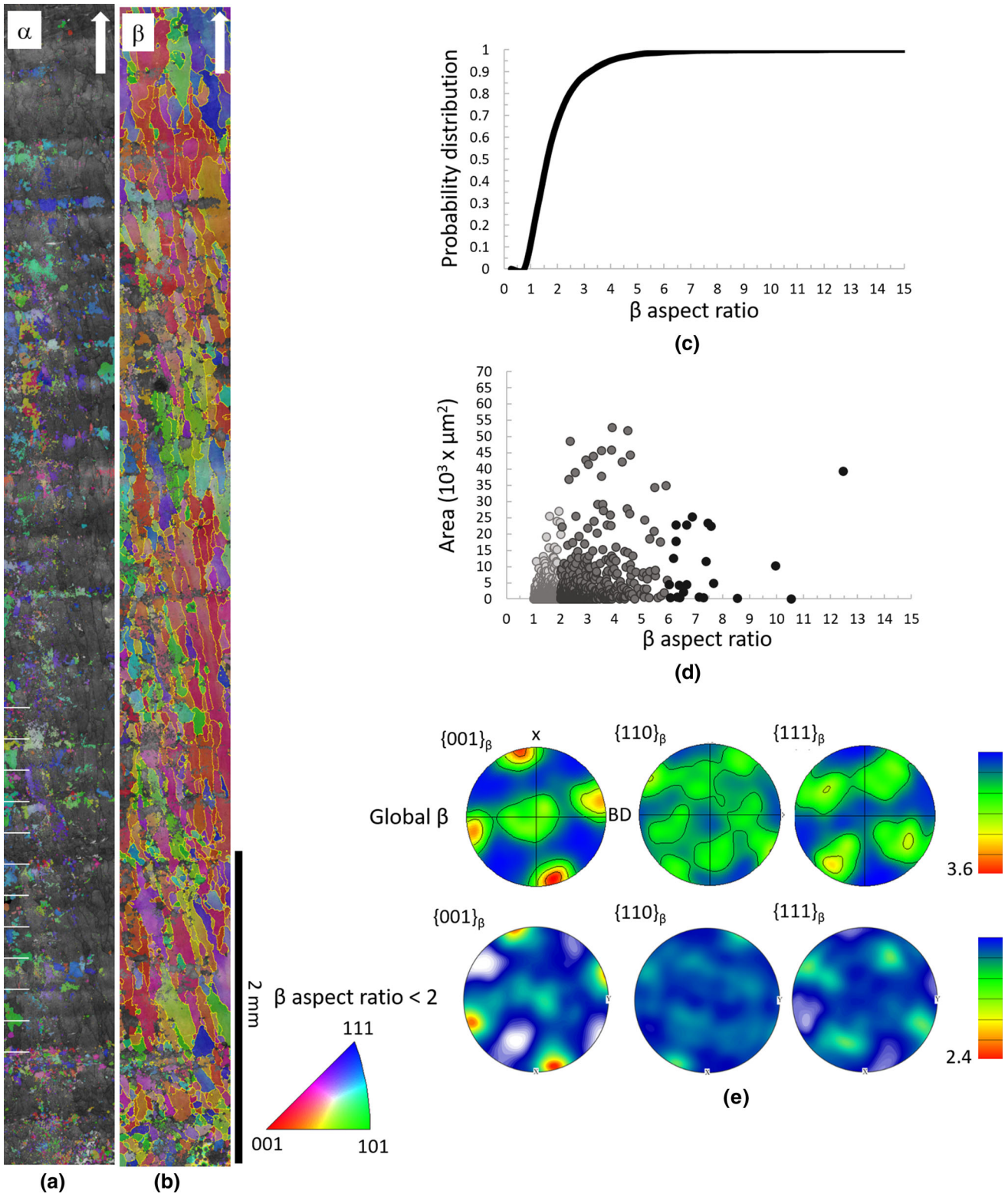
Fig. 3—(*a*) and (*b*) z-IPF orientation maps showing the distribution of the α and β phases in as-built Ti-6Al-4V-3Fe (white arrow is the build direction), respectively. Precipitation of the α/α′ occurs predominantly in bands parallel to the platform base as indicated by the white lines overlaid on the α-phase IPF orientation map. The aspect ratio of the β-phase grains is plotted as a (*c*) cumulative distribution and as a (*d*) scatter plot of area *vs* aspect ratio. The area of the grains with aspect ratio < 6 is plotted with gray markers; the texture components of the β phase are shown in the contour pole figures for global β-phase and β grain with aspect ratio < 2 (*e*).
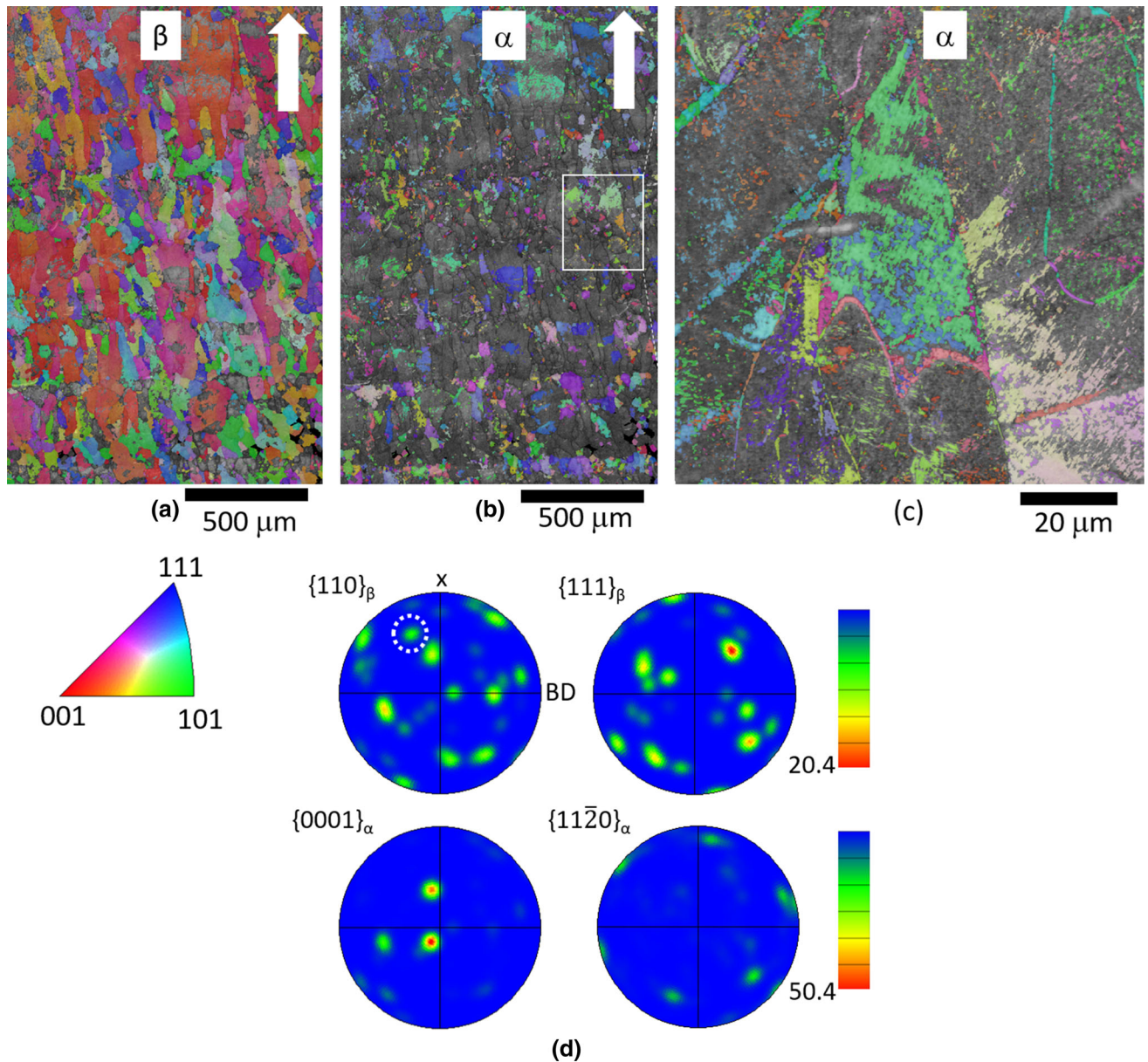
Fig. 4—Detailed orientation maps from Ti-6Al-4V-3Fe in the as-built condition (white arrows indicate the build direction). (*a*) and (*b*) z-IPF orientation maps of the *β* and *α* phases, respectively. (*c*) Enlarged area of a region in (*b*) showing details of *α* precipitation within *β*. The contour pole figures (*d*) indicate the orientation relationship between the *α* and *β* phases. Marked by a dotted white circle is an example of special reflection that does not find correspondence in the *α* contour pole figure.

constitutionally undercooled zone while embrittling the alloy. By leveraging the fact that titanium alloys naturally contain a population of native nucleant particles that can be exploited for grain refinement,[31] this present research demonstrates that Fe is a good solute for achieving significant *β* grain size reduction.

As reported in Table IV, the average partition coefficient of both Al and V in Ti approaches 1. For this reason, Al and V have limited contribution to the development of the constitutionally undercooled zone ahead of the L–S interface. On the other hand, Fe has an average partition coefficient of 0.33 and this, combined with higher values of liquidus slope, $m_l$, leads to significantly higher $Q$ values than is the case of

conventional Ti-6Al-4V ternary alloy which promotes the CET.

In addition, the rejection of Fe during solidification produces an increase in the predicted solidification range of the alloys (under both equilibrium and Scheil conditions where it is assumed no diffusion in the solid and complete mixing in the liquid) which also a condition necessary for the nucleation of new grains (Table V).

It is, however, observed that the rate of refinement decreases for Fe additions above 3 wt pct despite the increase in the corresponding calculated value of $Q$. This apparent contradiction can be explained considering that, for the refinement to occur, heterogeneous nuclei
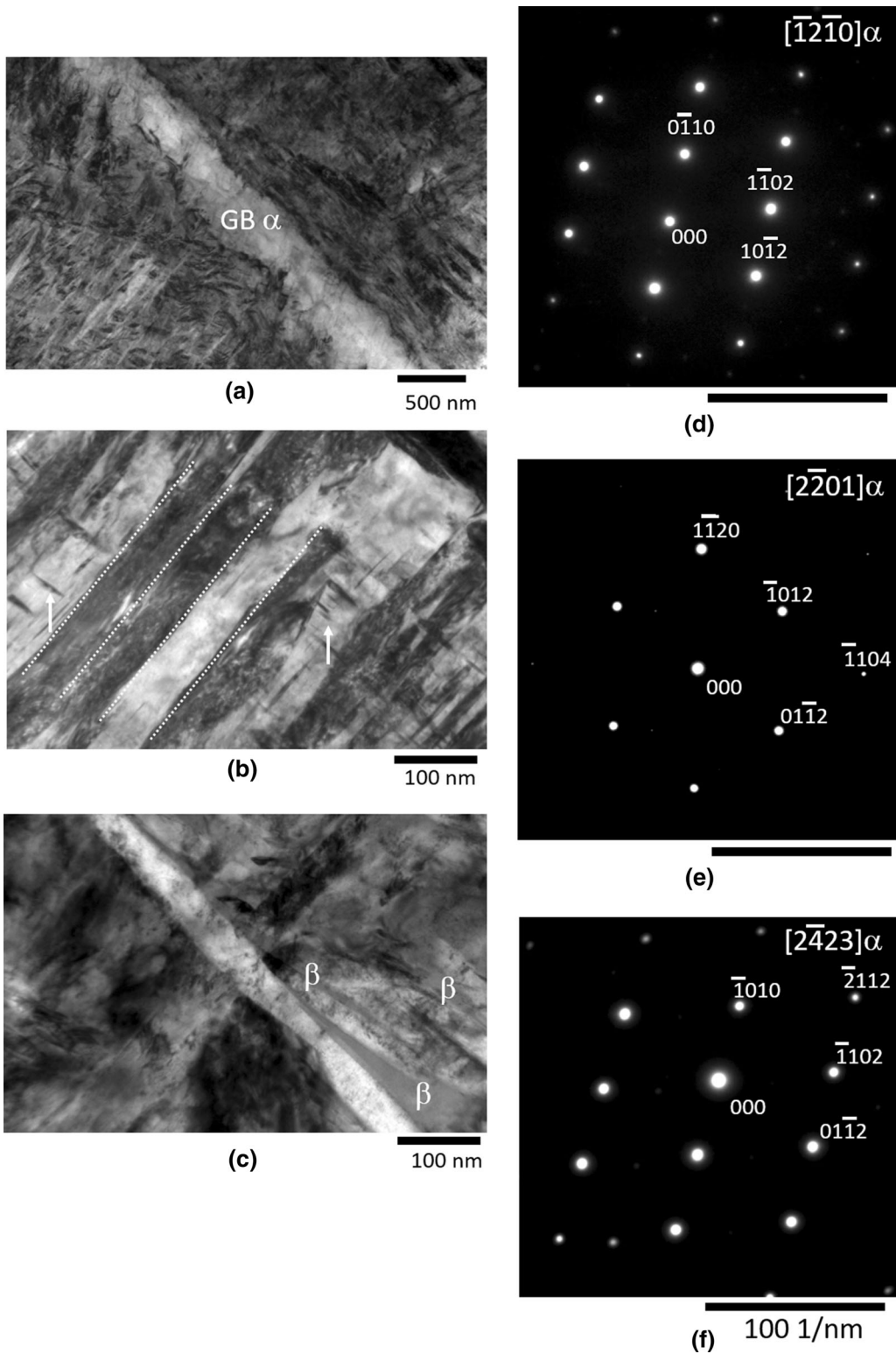
Fig. 5—Bright-field TEM micrographs of as-built Ti-6Al-4V-3Fe showing (*a*) the arrangement of GB α and the martensitic α′ phases. (*b*) A small α′ colony (dashed lines) and secondary and tertiary α′ indicated by arrows. (*c*) The interlaminar arrangement of retained β near the α′ phase. (*d*) to (*f*) SADPs recorded from individual α/α′ laths and their corresponding zone axis.

need to be present in the melt. As it is thought that only a limited number of native nuclei are available in the melt pool, these might be progressively consumed up to the point where further additions of Fe trigger no further grain nucleations. Remarkably, it is observed that refinement of the β phase takes place even if the negative enthalpy of mixing associated with the synthesis of TiFe is known to generate additional temperature

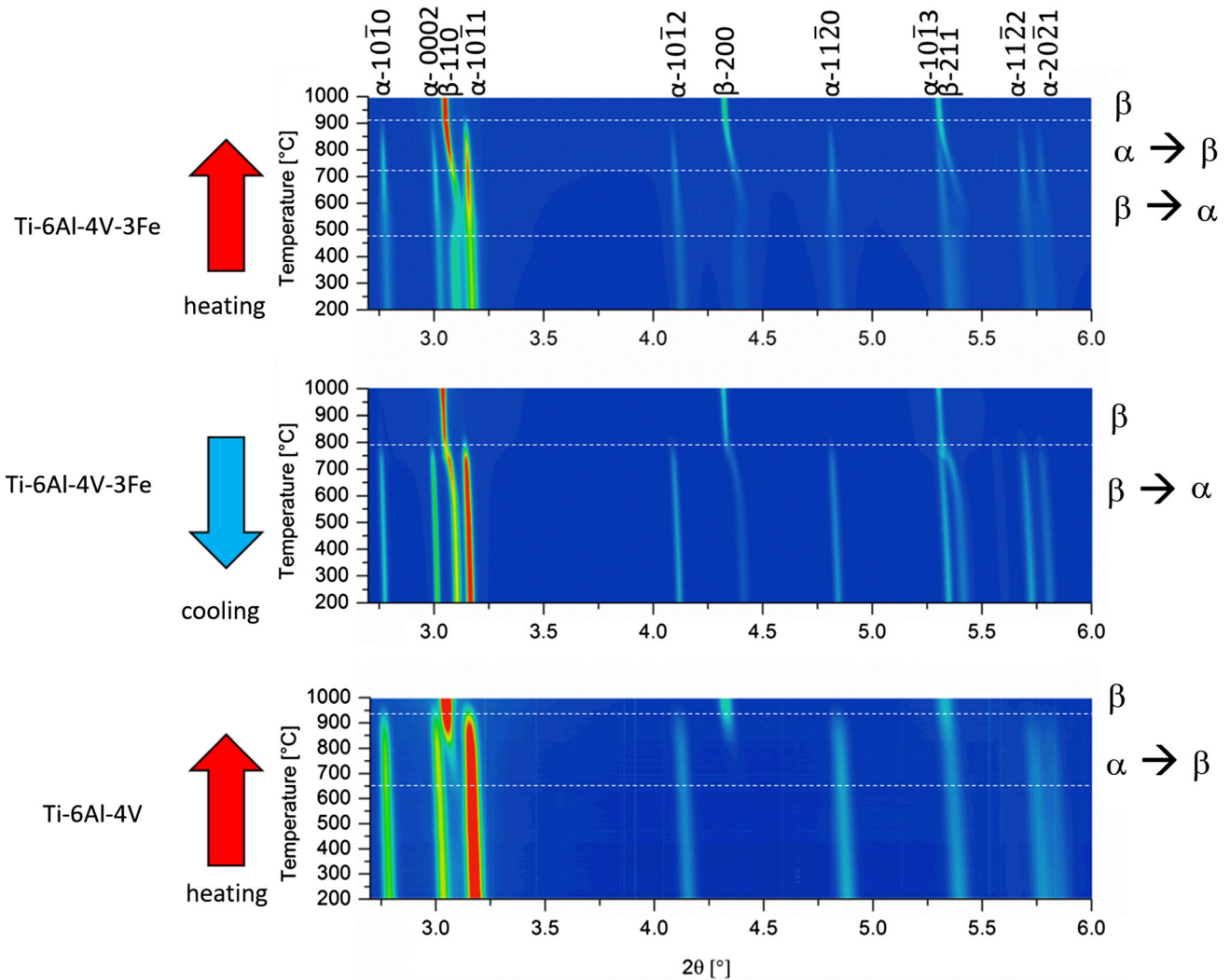| Microstructural Feature | Element (Wt Pct) | | | |
| --- | --- | --- | --- | --- |
| | Ti | Al | V | Fe |
| GB α | bal. | 6.4 ± 0.1 | 3.1 ± 0.1 | 2.2 ± 0.2 |
| α Laths | bal. | 6.3 ± 0.2 | 3.5 ± 0.1 | 2.9 ± 0.1 |
| β Laths | bal. | 5.7 ± 0.2 | 4.4 ± 0.1 | 4.4 ± 0.2 |



Fig. 6—Contour plots extracted from HEXRD patterns of the as-built Ti-6Al-4V-3Fe sample and a reference martensitic wrought Ti-6Al-4V, obtained during heating and cooling cycles at a rate of 100 °C/min. The plots reveal the evolution of {hkl} reflections of the α and β phases for a 2θ range of 2.25 to 6.0 deg.

rise in the melt pool,[27] which might increase the temperature gradient in the melt and so decrease the possibility to activate native nucleant particles.

The crystallographic analysis presented in Figure 3 allows more insights into the solidification mechanisms of Ti-6Al-4V-3Fe. The results show that the fine grains with apparent equiaxed morphology (as well as those with columnar morphology) possess a cube texture

component. This implies that the apparent equiaxed morphology of such fine grains is misleading and, in fact, fine grains have instead grown in a columnar dendritic mode. Since the cross-sections examined are not exactly parallel to the main axis of the grains, fine columnar grains would appear with equiaxed morphology on the plane of observation. Hence, caution is advised when interrogating such specimens with
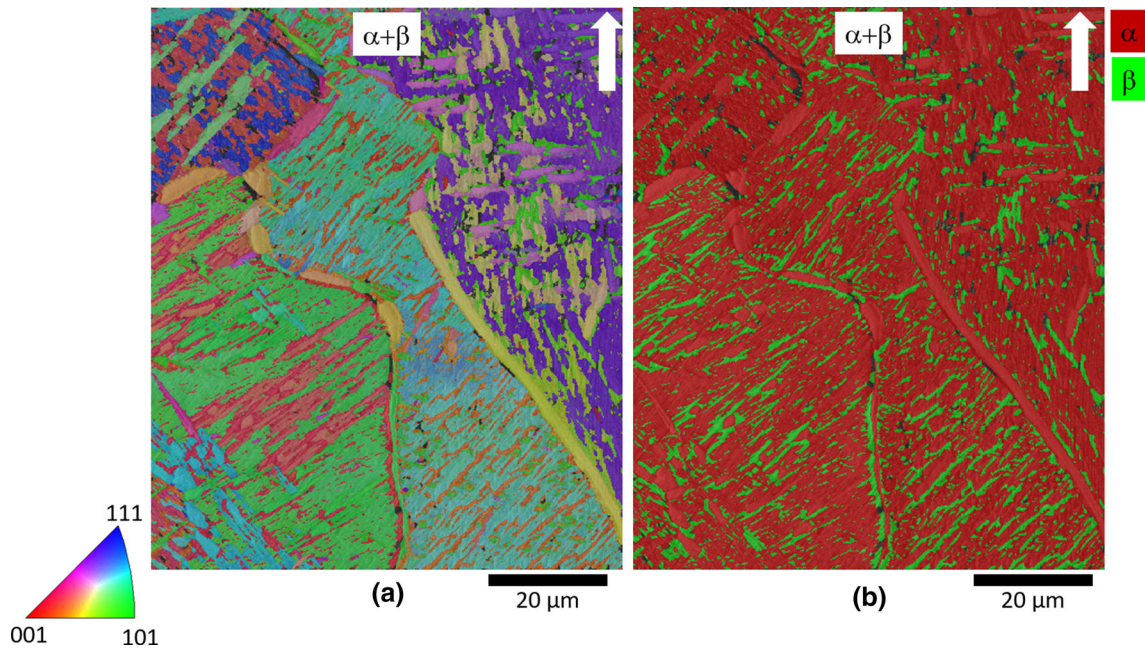
Fig. 7—Microstructure of Ti-6Al-4V-3Fe sample after a 4-hour heat treatment at 900 °C. The build direction is shown by the white arrow. (*a*) Overlaid z-IPF orientation maps of the α and β phases. (*b*) Overlaid phase maps showing α as red and β as green. Grain boundary α decorates the prior-β grains that comprise a fully lamellar α + β microstructure.



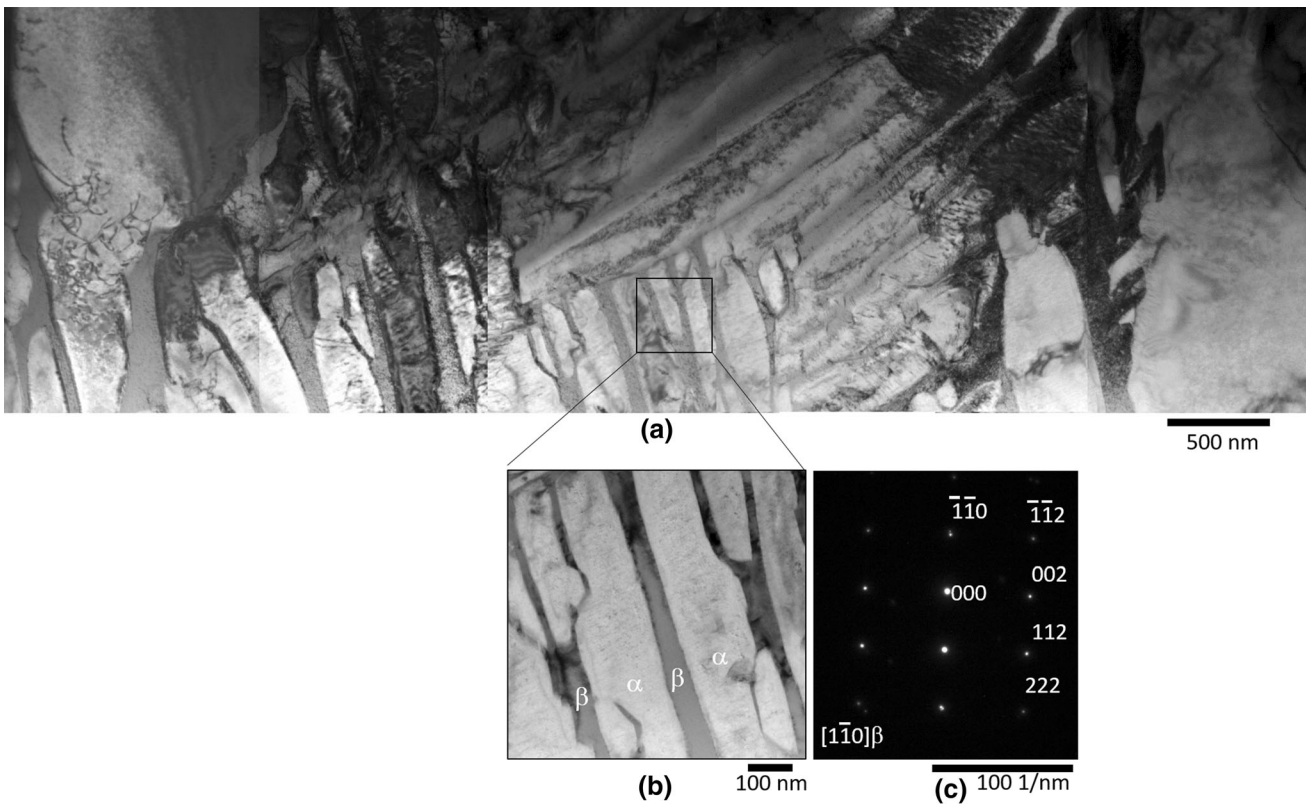Fig. 8—Bright-field TEM micrographs from Ti-6Al-4V-3Fe after a 4-h heat treatment at 900 °C. (*a*) α + β microstructure at low magnification. (*b*) α + β microstructure at higher magnification. (*c*) SADP obtained from a dark contrast region in (b) confirming the presence of β phase. There is no evidence for intermetallic compounds or ω phase in the regions of the heat-treated sample examined.

**Table III. The Average Composition Determined by TEM-EDX Point Analysis of the Microstructural Features Observed in the Ti-6Al-4V-3Fe Alloy After Heat Treatment at 900 °C Followed by Furnace Cooling**

| Microstructural Feature | Element (Wt Pct) | | | |
|---|---|---|---|---|
| | Ti | Al | V | Fe |
| GB α | bal. | 7.3 ± 0.8 | 1.4 ± 0.5 | 0.1 ± 0.02 |
| α Laths | bal. | 7.7 ± 0.1 | 1.4 ± 0.1 | 0.1 ± 0.03 |
| β Laths | bal. | 4.4 ± 0.6 | 7.4 ± 1.0 | 7.5 ± 1.0 |

**Table IV. Calculated Growth Restriction Factors $Q$ Associated to the Solutes Investigated in this Research in Titanium**

| Solute | $m_l$ | $c_0$ | $k$ | $Q$ |
|---|---|---|---|---|
| Al | 5 | 6 | 1.13 | 4 |
| V | − 3 | 4 | 0.86 | 2 |
| Fe | − 14 | 1 to 10 | 0.33 | 9 to 40 |

microscopy techniques based on 2D analysis. The lack of truly randomly oriented equiaxed grains might be related to the combined effect of a changing $G/R$ ratio across the melt pool and the layer-by-layer deposition. As shown in a number of related studies,[17,31] the combination of relatively higher $R$ and lower $G$ in the latter stages of the solidification of the melt pool might create the conditions to promote the nucleation of fine/equiaxed grains only near the free edge of each layer. However, during the successive layer deposition, this fraction of grains near the top of the previously solidified tracks are re-melted to re-grow epitaxially in the last deposited layer, leading to the development of the observed grain directionality.

Another noteworthy aspect is the correlation between the pronounced $\{001\}_\beta$ cube/fiber texture along the building direction and the formation of coarse prior-$\beta$ columnar grains in L-PBF and generally AM of Ti-6Al-4V.[4,9,32,46] It is generally observed that although, in the initial layers, equiaxed grains form from heterogeneous nucleation of the $\beta$ phase either on the build platform or on the metallic powders, the number of stray orientations of the $\beta$ phase decreases with sample height.[46,47] This means that Ti-6Al-4V is extremely efficient at eliminating the so-called unfavorable orientations associated with those columnar grains that are inclined to the building direction. It is likely that at least two factors might contribute to this phenomenon. Firstly, the variant selection at the prior-$\beta$ grain boundary and the texture inheritance (commonly observed in Ti-6Al-4V) effectively limit the number of possible orientations that the $\beta$ phase can assume at each layer.[9,47] Secondly, as discussed above, Al and V have limited diffusivity in liquid Ti and therefore are associated with a limited solute diffusion field around the growing $\beta$ dendrite tips. Under this condition, it is likely that the competitive grain growth of converging

dendrites might follow the classical model for directional solidification developed by Walton and Chalmers[48] whereby misaligned grains are effectively stifled by secondary dendrite arms emitted by the primary dendrites growing with $\{001\}_\beta$ cube/fiber texture. Recent studies have shown a greater complexity depending on whether the GB involves converging or diverging columnar grains. However, irrespective of this difference, growth of secondary and tertiary side branches is the mechanism that underpins elimination of misoriented grains. Evidently, the interaction between the solute concentration fields from neighboring dendrite tips which are misaligned must be involved. We suggest therefore that the rejection of Fe from the solid during solidification (Fe has a much smaller partition coefficient than Al or V) creates a diffusion field which inhibits side-branching overgrowth and consequently inhibits the mechanism of misoriented grain elimination. The net effect is that, in Ti-6Al-4V-3Fe, many more columnar grains persist in the build giving a more diffuse texture and smaller grain widths. The use of solutes with high diffusivity in liquid Ti seems therefore an effective strategy to limit the development of sharp crystallographic $\beta$ textures and simultaneously reduce the width of prior-$\beta$ grains in Ti alloys.

### B. Decomposition of the β Phase During L-PFB and Heat Treatment

It is well known that Fe is a potent $\beta$ stabilizer and that approximately 3.5 wt pct additions in pure Ti can cause retention of a metastable $\beta$ upon water quenching.[35] The overall composition measured in the present sample results in a molybdenum equivalent (Mo-eq) parameter of between 4 and 5 so it is not surprising to observe a $\beta$-rich $\alpha$ + $\beta$ structure in the as-built condition. Our research demonstrates, however, that a fraction of the $\beta$ phase observed at room temperature is metastable as a substantial amount of $\alpha$ phase precipitates after a post-build furnace heat treatment. This is derived from the high cooling rates imposed by the additive process and implies that a lower critical amount of Mo-eq elements (in this case Fe) are needed to pass through the martensite start temperature (Ms) curve under L-PBF conditions. Importantly, this also implies that upon cooling through the $\beta$ transus, $\alpha$ can nucleate at the $\beta$ grain boundaries and not almost exclusively from their grain interior as is the case of martensitic $\alpha'$ in Ti-6Al-4V.[9] This has similarities with the solidification

**Table V. The Solidification Range Corresponding to the Examined Ternary and Quaternary Alloys**

|  | Ti-6Al-4V | Ti-6Al-4V-2Fe | Ti-6Al-4V-3Fe | Ti-6Al-4V-4Fe |
|---|---|---|---|---|
| Solidification Range | 7 | 47 | 67 | 84 |

of $\alpha + \beta$ Ti alloys in additive processes that feature lower cooling rates (such as electron beam melting (EBM) and other powder- and wire-beam deposition techniques[13,49]) where it was shown that continuous precipitation of GB $\alpha$ decorates prior-$\beta$ grains.[24,27,30,50]

The subsequent thermal cycles of L-PBF involving the re-heating of previously deposited material associated with the deposition of additional layers would cause the precipitation of small $\alpha'$ colonies noted in the as-built structure. We observed a periodicity of the coarsening of these precipitates every $\sim 200$ $\mu$m indicating that each layer might experience at least ~3 thermal cycles with peak temperatures above the $\beta$-transus temperature. Besides reducing the chance to have equiaxed grains, the associated rapid heating and cooling of each thermal cycle causes the precipitation of secondary and tertiary $\alpha$, as recently suggested in Reference 1. Notably, Fe affects considerably the precipitation of the $\alpha'$ phase, as demonstrated by the fact that the colonies are not exclusively related to the surrounding $\beta$ phase by the well-known Burgers crystallographic orientation relationship (BOR) which dictates growth mechanics from parent crystals and is reflected in the element partitioning inferred from *in situ* HEXRD. Further studies to elucidate how the partitioning behavior of Fe is controlling the movement of the $\alpha/\beta$ interface or the recrystallization of the matrix are ongoing.

Upon heat treatment, a marked partitioning of the solutes and in particular that of Fe is observed (Table III), which derives from fast diffusion rates of Fe in both the $\alpha$ and $\beta$ phases.[35] This implies that, at least for heat treatments in the lower $\alpha + \beta$ region, phase transformations are essentially controlled by the partitioning of Fe. This study showed that after a 4-hour heat treatment at 900 °C, solutes partitioned entirely according to the predicted equilibrium solubility at room temperature. Interestingly, the investigation reveals the absence of $\omega$ phase, a deleterious phase that is known to form upon decomposition of metastable $\beta$.[34,35] The formation of $\omega$ phase is, however, rarely observed in the ternary alloy Ti-6Al-4V and for relatively low concentrations of $\beta$-stabilizers. The findings of this research suggest therefore that upon the proposed heat treatment, the $\alpha'$ and metastable $\beta$ phases (that dominate the structure in the as-built condition) decompose into a desirable and well-studied fully laminar $\alpha + \beta$ microstructural arrangement which is associated with an acceptable strength–ductility trade-off.

The mechanical anisotropy shown by AM Ti-based alloys is likely to arise from several contributing factors, such as residual stress, porosity, as well as grain structure and texture. Although, to the authors' knowledge, a precise quantification of the effect of such factors on the mechanical properties is still missing, it is credible to propose that controlling the average grain size and microstructural discontinuities in the built structures

can result in superior predictability of properties as an overall improvement in processability/stress accommodation. Moderate additions of Fe (up to $\sim 3$ wt pct) has resulted in a marked grain refinement with predominant grain structure with an aspect ratio $< 6$. This may generate sufficient distribution in grain size to dilute the impact on anisotropy and therefore lead to a more desirable balance of mechanical properties.[41]

## V. CONCLUSIONS

The identification of suitable solutes and inoculants for grain refining Ti-based alloys produced by laser powder-bed fusion is a complex multi-factorial challenge as it is necessary to consider not only how these participate to the dendritic solidification but also their supplemental effect on mechanical properties and manufacturability. This research has shown that simple but representative parameters such as the slope of the liquid line $m_l$, the partition coefficient of each solute $k$, and the diffusivity of the solutes in liquid Ti are useful to discuss the refinement of Ti-based alloys. This, together with other manufacturability considerations, has led to the development of a novel quaternary Ti-6Al-4V-3Fe. The evidence presented in this research suggests that:

- a mixed feedstock of pre-alloyed Ti-6Al-4V and smaller Fe powders can be used to generate a novel Ti-6Al-4V-3Fe alloy during L-PBF;
- $\beta$-grain refinement is sustained by the rejection of Fe during dendritic growth. $\beta$-grains have a mixed columnar and apparent equiaxed morphology;
- the lack of truly randomly oriented equiaxed grains might be related to the combined effect of changing $G/R$ ratio across the melt pool and the numerous thermal cycles experienced by each deposited layer;
- the use of solute Fe as a refiner does not lead to obvious formation of deleterious intermetallic compounds unlike other in the case of other refiners investigated in the literature;
- the as-built microstructure Ti-6Al-4V-3Fe can be easily decomposed to a well-known fully laminar $\alpha + \beta$ microstructure. The resulting microstructure is likely to combine a suitable balance of strength and ductility given the refined size of the prior-$\beta$ grains and laminar arrangement of $\alpha + \beta$ laths.

## OPEN ACCESS

## REFERENCES

1. J. Yang, Y. Hanchen, J. Yin, M. Gao, Z. Wang, and X. Zeng: *Mater. Des.*, 2016, vol. 108, pp. 308–18.
2. R. Sabban, S. Bahl, K. Chatterjee, and S. Suwas: *Acta Mater.*, 2019, vol. 162, pp. 239–54.
3. ASTM International. F2924-14 Standard Specification for Additive Manufacturing Titanium-6 Aluminum-4 Vanadium with Powder Bed Fusion. West Conshohocken, PA; ASTM International, 2014. https://doi.org/10.1520/F2924-14.
4. S. Liu and Y.C. Shin: *Mater. Des.*, 2019, vol. 164, p. 107552.
5. S. Ren, Y. Chen, T. Liu, and Q. Xuanhui: *Metall. Mater. Trans. A*, 2019, vol. 50A, pp. 4388–4409.
6. A.M. Anna, G. Fredriksson, I. Yadroitsev, and P. Krakhmalev: *Opt. Laser Technol.*, 2019, vol. 109, pp. 608–15.
7. C. Qiu, N.J.E. Adkins, and M.M. Attallah: *Mater. Sci. Eng. A*, 2013, vol. 578, pp. 230–39.
8. M. Simonelli, Y.Y. Tse, and C. Tuck: *Mater. Sci. Eng. A*, 2014, vol. 616, pp. 1–11.
9. M. Simonelli, Y.Y. Tse, and C. Tuck: *Mater. Trans. A*, 2014, vol. 45, pp. 2863–72.
10. M.J. Matthews, T.T. Roehling, S.A. Khairallah, Gabe.M. Guss, S.Q. Wu, M.F. Crumb, J.D. Roehling, and J.T. McKeown: *Procedia CIRP*, 2018, vol. 74, pp. 607–10.
11. T.T. Roehling, S.S. Wu, S.A. Khairallah, J.D. Roehling, S.S. Soezeri, M.F. Crumb, and M.J. Matthews: *Acta Mater.*, 2017, vol. 128, pp. 197–206.
12. S. Bontha, N.W. Klingbeil, P.A. Kobryn, and H.L. Fraser: *Mater. Sci. Eng. A*, 2009, vols. 513–514, pp. 311–18.
13. S.P. Narra, R. Cunningham, J. Beuth, and A.D. Rollett: *Addit. Manuf.*, 2018, vol. 19, pp. 160–66.
14. X. Wei, E.W. Lui, A. Pateras, M. Qian, and M. Brandt: *Acta Mater.*, 2017, vol. 125, pp. 390–400.
15. P. Nandwana, Y. Lee, C. Ranger, A.D. Rollett, R.R. Dehoff, and S.S. Babu: *Metall. Mater. Trans. A*, 2019, vol. 50A, pp. 3429–39.
16. B. Vrancken, L. Thijs, J.-P. Kruth, and J. Van Humbeeck: *J. Alloys Compd.*, 2012, vol. 541, pp. 177–85.
17. B. Vrancken, L. Thijs, J.-P. Kruth, and J. Van Humbeeck: *Acta Mater.*, 2014, vol. 68, pp. 150–58.
18. S.N. Tedman-Jones, S.D. McDonald, M.J. Bermingham, D.H. StJohn, and M.S. Dargusch: *J. Alloys Compd.*, 2019, vol. 778, pp. 204–14.
19. M.J. Bermingham, S.D. McDonald, M.S. Dargusch, and D.H. StJohn: *Scripta Mater.*, 2008, vol. 58, pp. 1050–53.
20. K.M. Ibrahim, A.H. Hussein, and M. Abdelkawy: *Nonferr. Met. Soc. China*, 2013, vol. 23, pp. 1863–74.
21. S. Mereddy, M.J. Bermingham, D.H. StJohn, and M.S. Dargusch: *J. Alloys Compd.*, 2017, vol. 695, pp. 2097–2103.
22. M.J. Bermingham, S.D. McDonald, D.H. StJohn, and M.S. Dargusch: *J. Alloys Compd.*, 2009, vol. 481, pp. L20–L23.
23. I. Yadroitsev, P. Krakhmalev, and I. Yadroitsava: *JOM*, 2017, vol. 69, pp. 2725–30.
24. P.C. Collins, R. Banerjee, S. Banerjee, and H.L. Fraser: *Mater. Sci. Eng. A*, 2003, vol. 352, pp. 118–28.
25. M.J. Bermingham, S.D. McDonald, D.H. StJohn, and M.S. Dargusch: *J. Mater. Res. Technol.*, 2011, vol. 24, pp. 1529–35.
26. Y.Z. Zhang, C. Meacock, and R. Vilar: *Mater. Des.*, 2010, vol. 31, pp. 3891–95.
27. R. Banerjee, P.C. Collins, and H.L. Fraser: *Metall. Mater. Trans. A*, 2002, vol. 33A, pp. 2129–38.
28. M.J. Bermingham, S.D. McDonald, and M.S. Dargusch: *Mater. Sci. Eng. A*, 2018, vol. 719, pp. 1–11.
29. S.A. Tamirisakandala, R.B. Bhat, J.S. Tiley, and D.B. Miracle: *Scripta Mater.*, 2005, vol. 53, pp. 1421–26.
30. M.Y. Mendoza, P. Samimi, D.A. Brice, B.W. Martin, M. Rolchigo, R. LeSar, and P.C. Collins: *Metall. Mater. Trans. A*, 2017, vol. 48A, pp. 3594–3605.
31. M.J. Bermingham, D.H. StJohn, J. Krynen, S.N. Tedman-Jones, and M.S. Dargusch: *Acta Mater.*, 2019, vol. 168, pp. 261–74.
32. P. Barriobero-Vila, J. Gussone, A. Stark, N. Schell, J. Haubrich, and G. Requena: *Nat. Commun.*, 2018, vol. 9, p. 3426.
33. K. Ueda, S. Nakaoka, and T. Narushima: *Mater. Trans.*, 2013, vol. 54, pp. 161–68.
34. H. Azizi, H. Zurob, B. Bose, S.R. Ghiaasiaan, X. Wang, S. Coulson, V. Duz, and A.B. Phillion: *Addit. Manuf.*, 2018, vol. 21, pp. 529–35.
35. I. Polmear, D. StJohn, J.-F. Nie and M. Qian: in *Light Alloys (Fifth Edition)*, I. Polmear, S. David, N. Jian-Feng and Q. Ma, eds., Butterworth-Heinemann: Boston, 2017, pp 369–460.
36. M. Simonelli, N.T. Aboulkhair, P. Cohen, J.W. Murray, A.T. Clare, C. Tuck, and R.J. Hague: *Mater. Charact.*, 2018, vol. 143, pp. 118–26.
37. ASM HandBook: *Volume 3 Alloy Phase Diagram*, ASM International, Materials Park, 1992.
38. ASTM International. E112-13 Standard Test Methods for Determining Average Grain Size. West Conshohocken, PA; ASTM International, 2013. https://doi.org/10.1520/E0112-13.
39. ASTM International. ISO/ASTM52921-13 Standard Terminology for Additive Manufacturing-Coordinate Systems and Test Methodologies. West Conshohocken, PA; ASTM International, 2013. https://doi.org/10.1520/isoastm52921-13.
40. J.D. Hunt: *Mater. Sci. Eng.*, 1984, vol. 65, pp. 75–83.
41. A.E. Wilson-Heid, Z. Wang, B. McCornac, and A.M. Beese: *Mater. Sci. Eng. A*, 2017, vol. 706, pp. 287–94.
42. Y. Matsukawa, I. Okuma, H. Muta, Y. Shinohara, R. Suzue, H.L. Yang, T. Maruyama, T. Toyama, J. Shen, Y. Li, Y. Satoh, S. Yamanaka, and H. Abe: *Acta Mater.*, 2017, vol. 126, pp. 86–101.
43. S.M. Kelly: Thermal and microstructure modeling of metal deposition processes with application to Ti-6Al-4V, Virginia Tech, 2004.
44. C.C. Murgau: Microstructure model for Ti-6Al-4V used in simulation of additive manufacturing, Luleå tekniska universitet, 2016.
45. D.G. McCartney: *Int. Mater. Rev.*, 1989, vol. 34, pp. 247–60.
46. S.S. Al-Bermani, M.L. Blackmore, W. Zhang, and I. Todd: *Metall. Mater. Trans. A*, 2010, vol. 41A, pp. 3422–34.
47. A.A. Antonysam, J. Meyer, and P.B. Prangnell: *Mater. Charact.*, 2013, vol. 84, pp. 153–68.

48. D. Walton and B. Chalmers: *Trans. AIME*, 1959, vol. 215, pp. 447–57.
49. B.E. Carroll, T.A. Palmer, and A.M. Beese: *Acta Mater.*, 2015, vol. 87, pp. 309–20.
50. K.I. Schwendner, R. Banerjee, P.C. Collins, C.A. Brice, and H.L. Fraser: *Scripta Mater.*, 2001, vol. 45, pp. 1123–29.